ARTICLE OPEN

Dynamical and moist thermodynamical processes associated with Western Ghats rainfall decadal variability

Subrota Halder [1,2 ✉], Anant Parekh[1], Jasti S. Chowdary [1] and C. Gnanaseelan [1]

The Western Ghats (WG) is a vast montane forest ecosystem known for its biodiversity and endemism. The decadal variability of WG summer monsoon rainfall is higher than most of the other regions of India. Spectrum and wavelet analysis of century-long rainfall observation confirm significant decadal variability (at 90% confidence level) in WG rainfall, with amplification of magnitude (about 1.5–2 times) in the recent years compared to the previous half-century. Correlation analysis of WG rainfall with Indian (Pacific) Ocean sea surface temperature (SST) shows a significant relationship during 1901–1942 (1943–1977 and 1978–2010). The analysis associated with decadal rainfall variability reveals the dominance of dynamical processes during 1901–1942 and moist thermodynamical processes during 1943–1977 and 1978–2010. The study concludes that decadal variability of WG rainfall is robust and the forcing mechanisms are essentially maintained by the Indian and Pacific Oceans variability, adding value in developing decadal prediction systems and may also contribute towards understanding the evolution of WG ecosystem.

INTRODUCTION

Indian summer monsoon rainfall (ISMR) exhibits spatial and temporal variability, including diurnal to decadal scale[1–3], which are strongly linked to different oceanic and land surface phenomena[4–9]. The spatial distribution of ISMR shows high rainfall along Western Ghats (WG) and the Eastern Ghats, moderate rainfall in central India, and low rainfall towards northwest India[10]. WG is a north-south-oriented mountain range having narrow zonal width and a maximum height exceeding 2650 m, and the average elevation is 1200 m. WG form one of the four watersheds of India, feeding the perennial rivers of India. The Godavari, Kaveri, Krishna, Thamiraparani, and Tungabhadra are major river systems originating in the WG[11]. Majority of streams draining WG join these rivers and carry a large volume of water during the monsoon months. There are more than 50 major dams along WG[12]. The mountain chain of WG comprises unique biophysical and ecological processes and is home to more than 325 globally threatened flora, fauna, bird, amphibian, reptile, and fish species. WG represents one of the best examples of the monsoon system on the earth by moderating the Indian Monsoon system through its vast montane forest ecosystem. It is important to note that WG is recognized as UNESCO world heritage center for its biodiversity and endemism[13] and one of the world's eight 'hottest hotspots' of biological diversity along with Sri Lanka.

According to previous study[14], the cross-equatorial low-level monsoon jet (LLJ) carries a large amount of moisture from the southern Indian Ocean and the Arabian Sea (AS), gets lifted up, and pours them as heavy rainfall over WG. The mountain chain lies almost perpendicular to LLJ and hence, acts as a barrier, resulting in orographic rainfall, and so WG receives about three times the average rainfall of India[14–17] and about 90% of its annual rainfall during the Indian summer monsoon season[18]. These mountain ranges receive high rainfall, with an average annual rainfall of about 380 cm on the windward side[19]. The maximum rainfall on the windward side of WG occurs not at the line of maximum height but 5–10 km ahead of the maximum height[20]. Thus, from

the west coast, rainfall increases along the slopes of WG and rapidly decreases on the eastern leeward side due to the sinking air[21]. Summer monsoon rainfall of all the three subdivisions of WG shows significant positive correlations with all-India rainfall; the strength of correlation increases from south to north[22]. On average, 50% of the seasonal rainfall over WG is contributed by days with heavy rainfall spells[23]. According to Mooley[24], WG appears to play a differential role and contributes to the observed major discontinuities in monsoon activity. The factors such as the stationary gentle forced ascent of moisture-laden south-westerly monsoon winds over WG with additional ascent provided by transient synoptic, mesoscale systems contribute to the occurrence of high rainfall over the eastern AS, coastal area, and on WG mountains[14,19,20,25–28]. Two independent studies[29,30] suggested that the rainfall over the west coast of India is consistently decreasing. Previous studies[17,31,32] also reported a negative trend in WG summer precipitation. A recent study[22] examined the latitudinal variation of ISMR in different subdivisions of WG with the main focus on changes in ISMR and epochal behavior of those changes in the centennial time scale. They also discussed the impact of Indian Ocean Dipole (IOD) and Niño SSTs on rainfall during individual monsoon months. A significant increase in rainfall over the northern parts of the west coast of India and a decrease over north India are attributed to the variations in the west Pacific Ocean (120°E–150°E, 10°S–20°N) and the western Indian Ocean (40°E–70°E, 10°S–20°N) SST respectively during the period 1970–2014[33]. Joshi and Pandey[34] found a 15-year cycle for the southwest region rainfall, and from correlation, with SSTs they inferred that the warm phase of Atlantic Multidecadal Oscillation (AMO) and cold phase of Interdecadal Pacific Oscillation (IPO) enhance rainfall over the southwest region. Using long-term observational data, another study[35] also showed a strong positive correlation between AMO and the rainfall over the WG and AS region. It is important to note that the past studies were mostly based on different grid-size/areas and different data sources, leading to some differences in their conclusions. However, the

---
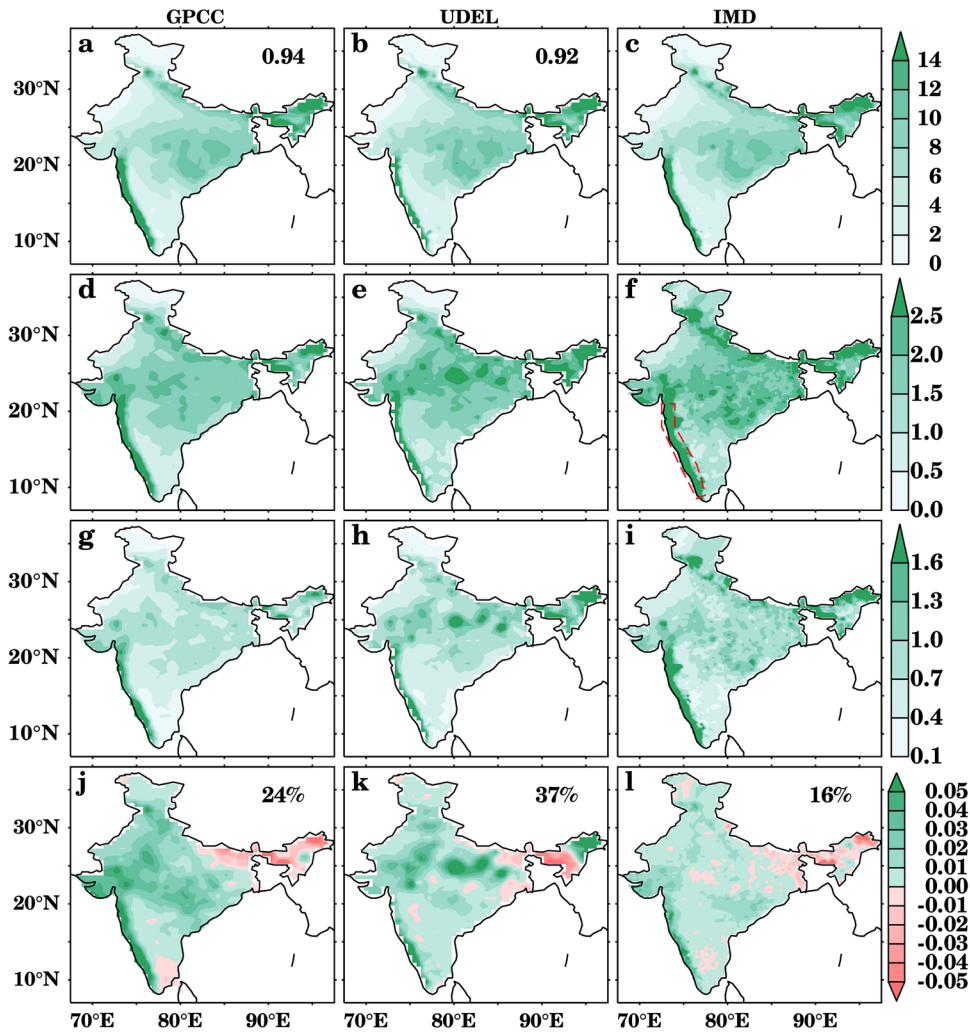
Fig. 1 Spatial distribution of mean and variability of summer monsoon rainfall over India. Spatial distribution of long-term mean summer monsoon rainfall (mm/day) from **a** GPCC, **b** UDEL, and **c** IMD. Numerical values in the right top corner in **a** and **b** showing pattern correlation with **c** IMD data. The standard deviation of summer monsoon rainfall (mm/day) from **d** GPCC, **e** UDEL, and **f** IMD and standard deviation of 9–30 years bandpass filtered summer monsoon rainfall (mm/day) from **g** GPCC, **h** UDEL, and **i** IMD. EOF leading first mode of 9–30 years bandpass filtered rainfall anomaly over Indian landmass from **j** GPCC, **k** UDEL, and **l** IMD. The percentage of total variability explained by EOF1 is shown in the top right corner in **j**, **k**, and **l**. The selected area in **f** using dashed lines representing the domain considered for Western Ghats rainfall index (WGI).

evolution of monsoon rainfall statistics over WG through the 20th century is dominated by variations in the interannual to interdecadal time scale. It is worthwhile to re-examine this problem using a longer time-series of rainfall data. It is also important to examine its link with the SST variations over the global ocean and the associated mechanisms using recently released century reanalysis data.

RESULTS

Interannual and decadal variability of Western Ghats rainfall

Figure 1a–c shows the June–July–August–September (JJAS, summer) mean rainfall/precipitation climatology over the Indian subcontinent from three different datasets: Global Precipitation Climatology Centre (GPCC), University of Delaware (UDEL), and India Meteorological Department (IMD). Central India, the WG, and the Meghalaya region recorded maximum seasonal precipitation during the summer monsoon. Figure 1d–f shows the standard deviation of summer monsoon rainfall; the WG region displayed 1.7–1.9 mm/day standard deviation, which is consistent in all three datasets. Figure 1g–i shows the standard deviation of 9–30 years

bandpass filtered summer monsoon rainfall anomaly. The maximum rainfall variability (0.8–0.9 mm/day) is seen in the WG and some parts of Central India and North-Eastern India. The normalized standard deviation for filtered WG rainfall anomaly (Supplementary Fig. 1) also confirmed the noticeable amplitude of decadal variability over the WG. EOF analysis of the bandpass filtered summer monsoon rainfall anomaly for all India reveals that the decadal variance of rainfall has significant strength over the monsoon core zone and WG (Fig. 1j–l), which is consistent with the finding of Vibhute et al.[3]. The above analysis suggests the presence of strong observed decadal to multidecadal variability over the WG region, followed by North Eastern and Central India, which is consistent in all three datasets. Considering the maximum rainfall and highest variability on the decadal scale over the WG, it is a prerequisite to explore the processes responsible for such a strong rainfall variability.

Figure 2a shows the time-series of WG precipitation index (WGI) from GPCC, UDEL, and IMD datasets; they displayed high coherence with each other. The intercorrelation of WGI are 0.94, 0.95, and 0.92 for GPCC-UDEL, GPCC-IMD, and UDEL-IMD respectively, supporting interconsistency in the WGI among the
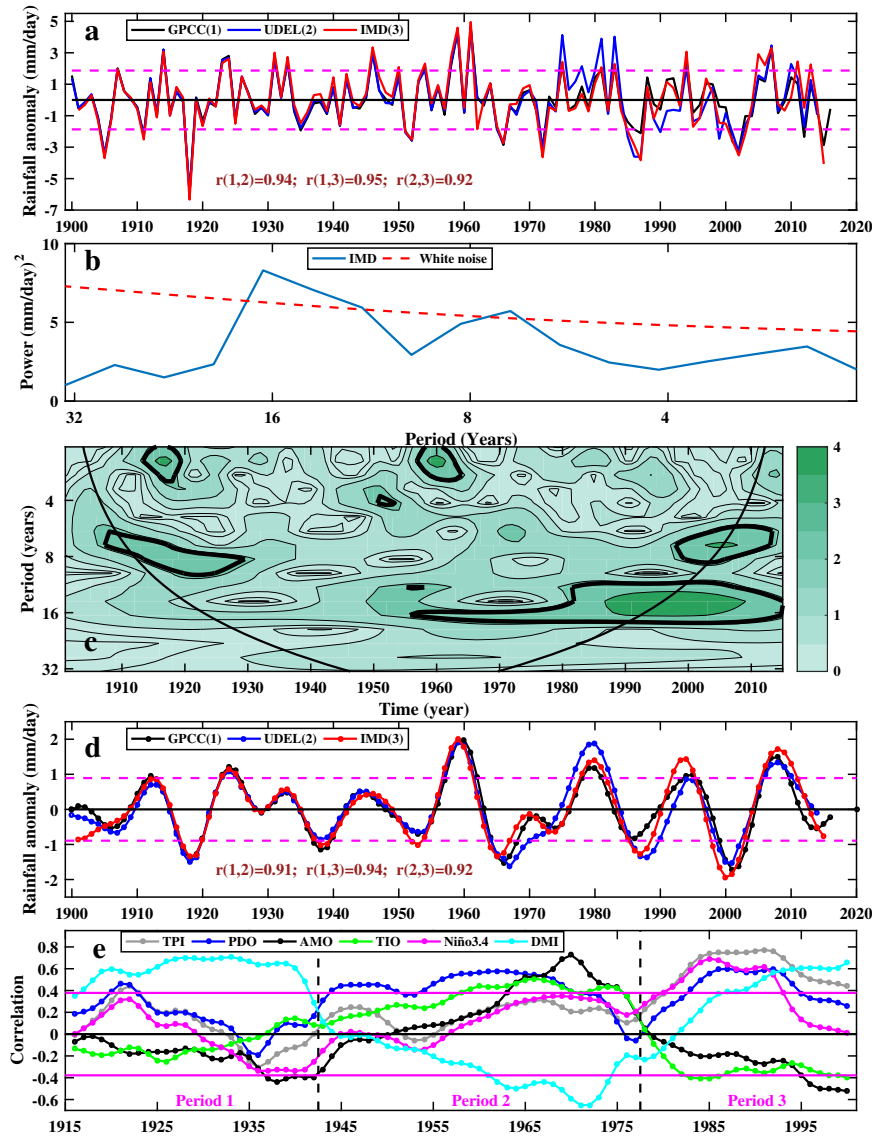
Fig. 2 Temporal evolution of rainfall variability over WG. a Time-series of summer monsoon rainfall anomaly (mm/day) over the Western Ghats (WG) from different rainfall datasets. Dashed lines indicate ±1 std of rainfall anomaly over the WG from IMD. **b** Power spectrum of IMD rainfall anomaly of WG. The dashed line displays white noise spectrum at 90% confidence level. **c** Wavelet spectrum of IMD rainfall anomaly of WG. Black thick solid line contours indicate signal qualifies 90% confidence level. **d** 9–30 years bandpass filtered summer monsoon rainfall anomaly (mm/day) over the WG from different datasets. Dashed magenta color lines are ±1 std of filtered rainfall anomaly from IMD. **e** 31-years running correlation of 9–30 years bandpass filtered WGI with different filtered SST indices manifest major climate variability over the different parts of the global ocean. The solid magenta line represents the 90% confidence level for the correlation.

rainfall datasets and confirming the robustness of the WG rainfall variability. Figure 2b shows the power spectrum of WGI from IMD rainfall. The red dashed line shows white noise with 90% confidence. Spectrum analysis of WGI shows two peaks crossing the 90% confidence level; corresponding periods of peaks are 7 years and 12–20 years (with maximum strength at 17 years), respectively, confirming the decadal and multidecadal variability when considering the entire time-series. Figure 2c shows the wavelet analysis of WGI, where the y-axis is frequency/period and the x-axis is time; different color shades display the strength of the signal of a particular frequency at that time. However, it is crucial to know whether the strength of frequency is statistically significant or not, for which white noise spectrum analysis is applied at a 90% confidence level. The black thick line contour displayed in Fig. 2c indicates the strength of this frequency/period is qualifying the significant test. According to which, 6–10-year period was significant during 1908–1930 and also during

1998–2012; in the recent period, decadal to multidecadal variability in 12–20-year time period is dominant during 1956 to 2015. Above spectrum and wavelet analysis is the basis to apply 9–30 years bandpass filtered to WGI from GPCC, UDEL, and IMD datasets for extracting decadal and multidecadal signals (Fig. 2d). Similar to interannual variability (Fig. 2a), decadal variability strength is high after 1955 compared to the earlier period. The horizontal dashed magenta lines show ±1 standard deviation for the index from the IMD dataset. Those years when WGI is greater/smaller than one standard deviation are considered extremes; for positive they are excess years, and for negative they are deficit years. Figure 2d also shows the correlation between different datasets for WGI decadal to multidecadal variability, and it has a correlation of 0.91, 0.94 and 0.92 for GPCC-UDEL, GPCC-IMD, and UDEL-IMD respectively. Individual SST indices with WGI are shown as Supplementary Fig. 3.

Table 1.	Excess and deficit precipitation year for different periods.	
Period	Excess years	Deficit years
Period 1 (1901–1942)	1923, 1924	1917, 1918, 1919, 1920; 1938, 1939
Period 2 (1943–1977)	1957, 1958, 1959, 1960, 1961	1965, 1966, 1967
Period 3 (1978–2010)	1980, 1981; 2006, 2007, 2008, 2009, 2010	1986, 1987; 1999, 2000, 2001, 2002, 2003

Relationship of WG rainfall variability with dominant SST modes

To identify the relationship between WGI and the dominant mode of SST variability over the world ocean, 31-years moving correlation analysis (Fig. 2e) is performed on filtered WGI and filtered SST indices i.e., Tri-Polar Index[36] (TPI) for IPO, Pacific Decadal Oscillation[37] (PDO), AMO[38], Tropical Indian Ocean (TIO) basin mode index[39], Niño 3.4 for El Niño Southern Oscillation and Dipole Mode Index (DMI) for IOD. It shows changes in the relationship of WGI decadal variability with SST indices. WGI displayed a significant positive correlation with DMI during 1901–1942. PDO modulated WG rainfall variability during 1942–1972 and 1980–1994 and is in phase with a significant correlation of about 0.6. The phase relationship underwent some changes after 1983 where Niño3.4, PDO, DMI are all positively correlated, and TIO, AMO are negatively correlated. From this analysis, it is clear that there is a change in the relationship between WGI decadal variability and SST Indices around 1942–43 and 1977–78. A recent study by Preethi et al., Figure 4a[33] found similar epochal changes in low-frequency variability of rainfall over the west coast of India. The sensitivity of the above-discussed result to the bandpass filter window supports that the classification of time span in the selected three periods is well separated and insensitive to bandpass filters window. However, some difference is reported for AMO index to bandpass filter window. Therefore, the decadal rainfall variability of WG is studied separately for three periods: period 1 (1901–1942), period 2 (1943–1977), and period 3 (1978–2010). Table 1 listed excess and deficit years for each period, which are the years having WGI amplitude greater/lesser than 1 standard deviation. Period-wise regression, correlation, and composite analysis for excess and deficit years is carried out to understand the role of circulation and thermodynamical processes.

Composite analysis of WG rainfall and SST for excess and deficit years

Figure 3 shows the composite of summer monsoon precipitation anomaly for excess and deficit years and their difference for each period. During the first period, excess years composite (Fig. 3a) displays a positive anomaly of rainfall over the southern part of WG, and during deficit rainfall years, negative rainfall anomaly (Fig. 3b) is seen over the entire WG. So apparently, the difference in excess and deficit years is confined over the southern part of WG with an anomaly of 6.5 mm/day or more (Fig. 3c). In period 2 (Fig. 3d–f), a pattern of anomalous rainfall is different from period 1. Positive and negative rainfall anomalies for respective composite covers the entire WG region with anomalies of 0.5–5 mm/day. During period 3 (Fig. 3g–i) excess years, positive rainfall anomalies are found over the entire WG region except the southernmost region, but deficit years displayed negative rainfall anomalies along the entire WG region. Spatial pattern of rainfall anomaly for excess and deficit remains unchanged to different bandpass filter.

Figure 4 shows the composite of summer SST anomaly (SSTA) from Extended Reconstructed Sea Surface Temperature version-5 (ERSSTv5) for excess and deficit years for different periods. Contours in Fig. 4c, f, i show the correlation coefficient of filtered WGI with filtered SST at 90% confidence level, with solid (dashed) lines showing positive (negative) correlation values. In period 1,

composite SSTA for excess rainfall years (Fig. 4a) shows a positive IOD pattern and a negative IOD pattern for deficit rainfall years (Fig. 4b). This analysis further suggests that apart from IOD, Pacific Ocean SSTA also shows the coherent response with WGI, and the pattern of anomaly has some resemblance with the PDO pattern. However, associated signals in the eastern equatorial Pacific SSTA are out of phase (Fig. 4c), which is also supported by the correlation analysis of WGI with SSTA. In period 2 (Fig. 4d–f), a positive (weak negative) PDO type pattern is observed over the Pacific Ocean for excess (deficit) rainfall years; however, IOD signal is absent in the Indian Ocean. Spatial pattern of significant correlation (Fig. 4f) shows PDO pattern, where WGI is positively correlated with north-eastern Pacific and negatively correlated with the north-central Pacific. Figure 4g–i shows the SSTA composite for excess and deficit years during period 3. IPO displayed a transition from positive to negative phase around 1999–2000[40], and so SSTA composites in the two IPO phases are also studied. Post-2000 composite is given in Supplementary Fig. 4. Composite analysis shows IPO/PDO type SSTA pattern, positive IPO/PDO pattern supports excess phase and vice versa prior 2000 (figure not shown). Krishnan and Sugi (2003) carried out a diagnostic analysis of historical climate datasets to study the influence of the Pacific Ocean decadal variability on ISMR. Their findings suggest an inverse relationship between the Pacific SST variations associated with the PDO and ISMR. The correlation map of SSTA with WGI also displayed IPO type pattern in the Pacific Ocean and IOD type pattern in TIO for the period 1978-2000, with the confidence level of 90%. An opposite pattern of SSTA for excess and deficit composite is evident (Supplementary Fig. 4) for the post-2000 analysis.

Regression analysis of dynamical and thermodynamical parameters with WGI

Figure 5a–c shows regression of WGI with low-level wind anomaly and vertical wind anomaly (Fig. 5a), with vertically integrated moisture transport (VIMT) anomaly and vertically integrated moisture (VIM) anomaly (Fig. 5b), with tropospheric temperature anomaly and moist static energy (MSE) anomaly (Fig. 5c) for period 1. Corresponding correlation analysis and composite analysis for excess and deficit years and their differences are displayed in Supplementary Fig. 5a–c and 6 respectively. Regression and correlation analysis reveals that the significant relation qualifies 90% confidence level with low-level monsoon circulation over the AS and associated moisture transport; however, significant relation is found for the troposphere temperature and MSE over central India and monsoon trough region. With all these fields, correlation is carried out with the WGI for period 1 (Supplementary Fig. 5a–c), which displays a significant correlation with the monsoon circulation fields. However, for MSE, a high correlation is found over northwest India. The composite analysis of low-level winds during excess years shows anomalous easterly winds near the equator associated with positive IOD[41] turn towards right and converge over WG as a response to east equatorial cooling followed by a Matsuno-Gill type mechanism[42,43]. Westerlies all along the latitudes of WG with a positive magnitude of 2 m/s and positive vertical wind anomaly with high (3×10^{-3} m/s) anomaly north of 10°N are found during the excess years (Supplementary Fig. 6a), however, during deficit
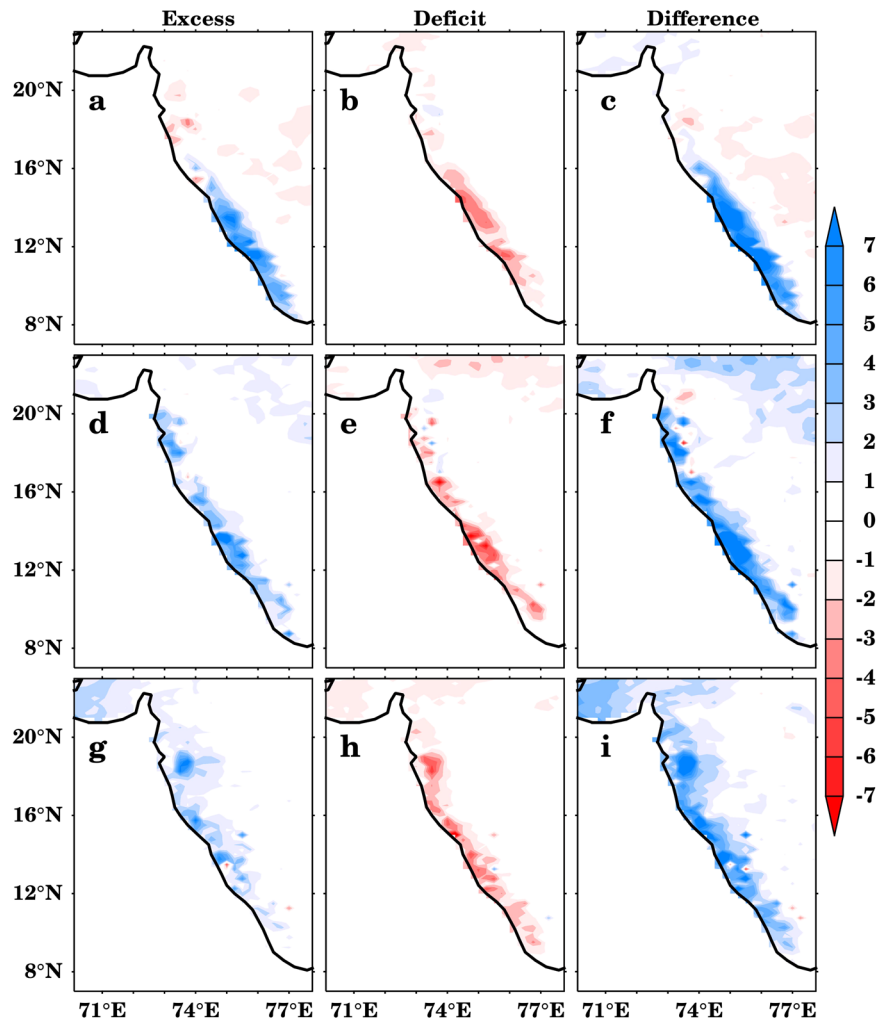
Fig. 3 Spatial distribution of rainfall over WG for excess and deficit phases. Composite of summer monsoon rainfall anomaly (mm/day) over WG from IMD for **a** excess, **b** deficit years, and **c** their difference (**a**, **b**) for period 1 (1901–1942). **d**, **e**, and **f** same as **a**, **b**, and **c** but for period 2 (1943–1977). **g**, **h**, and **i** same as **a**, **b**, and **c** but for period 3 (1978–2010).

years, WG experienced easterly wind anomalies and negative vertical wind anomalies (Supplementary Fig. 6b). The difference (Supplementary Fig. 6c) shows that the convergence of westerly winds toward WG and associated positive vertical wind anomaly is visible. Similarly, the composite of VIMT and VIM anomalies (Supplementary Fig. 6d–f) in excess years shows anomalous VIMT flow towards WG from equatorial western Indian Ocean and AS, whereas, in deficit rainfall years, anomalous moisture transport is out of WG region, towards the ocean. This VIMT anomalies are consistent with excess (deficit) rainfall occurrence in period 1, which is also clearly seen in the difference (Supplementary Fig. 6f). The Tropospheric Temperature (TT) excess and deficit composite (Supplementary Fig. 6g–i) is not much different, high TT is reported over northwest India and negative over the tropical Indian Ocean in the difference. Monsoon-associated heating is represented by TT anomaly, and its meridional gradient maintains large-scale monsoon circulation[44–47]. MSE for both phases shows weak anomalies resulting in a positive MSE difference over northwest India during period 1. Hence, regression, correlation, and composite analysis support that during period 1, circulation associated with monsoon is primarily responsible for the rainfall variability and moisture transport and MSE plays a secondary role.

Figure 5d–f shows regression of WGI with low-level wind anomaly, vertical velocity (Fig. 5d), with VIMT anomaly and VIM anomaly (Fig. 5e), with tropospheric temperature anomaly and

MSE anomaly (Fig. 5f) for period 2. This analysis shows significant relationship between low-level circulation north of Madagascar and over the Somalia region, whereas VIMT, VIM, tropospheric temperature, and MSE displayed significant regression almost over the entire AS and WG region apart from some part of Bay of Bengal and monsoon trough region. Supplementary Fig. 7 shows the composite analysis similar to Supplementary Fig. 6 but for period 2. Low-level wind (Supplementary Fig. 7a–c) is weak westerly over the WG region for excess precipitation years and weak easterly for deficit years. The vertical wind (at 500 hPa) anomaly is positive throughout WG, central India, over the southeastern AS and eastern equatorial the Indian Ocean for excess years, and negative over most of the region except some part of northeast India and eastern equatorial the Indian Ocean for deficit years. In the difference (Supplementary Fig. 7c), westerly anomaly (~3 m/s) and positive vertical wind anomaly are seen over WG and central and north India, exhibiting intense monsoon activity over the region. VIMT anomaly (Supplementary Fig. 7d–f) is towards WG for excess year composite and away from WG for deficit year composite. Similarly, the VIM anomaly is positive (negative) over the whole of India for excess (deficit) years; the difference between the two composites is positive north of the equator (Supplementary Fig. 7f), which indicates more moisture transport favoring excess rainfall. The lower panel (Supplementary Fig. 7g–i) shows the composite of TT and MSE anomaly for excess,
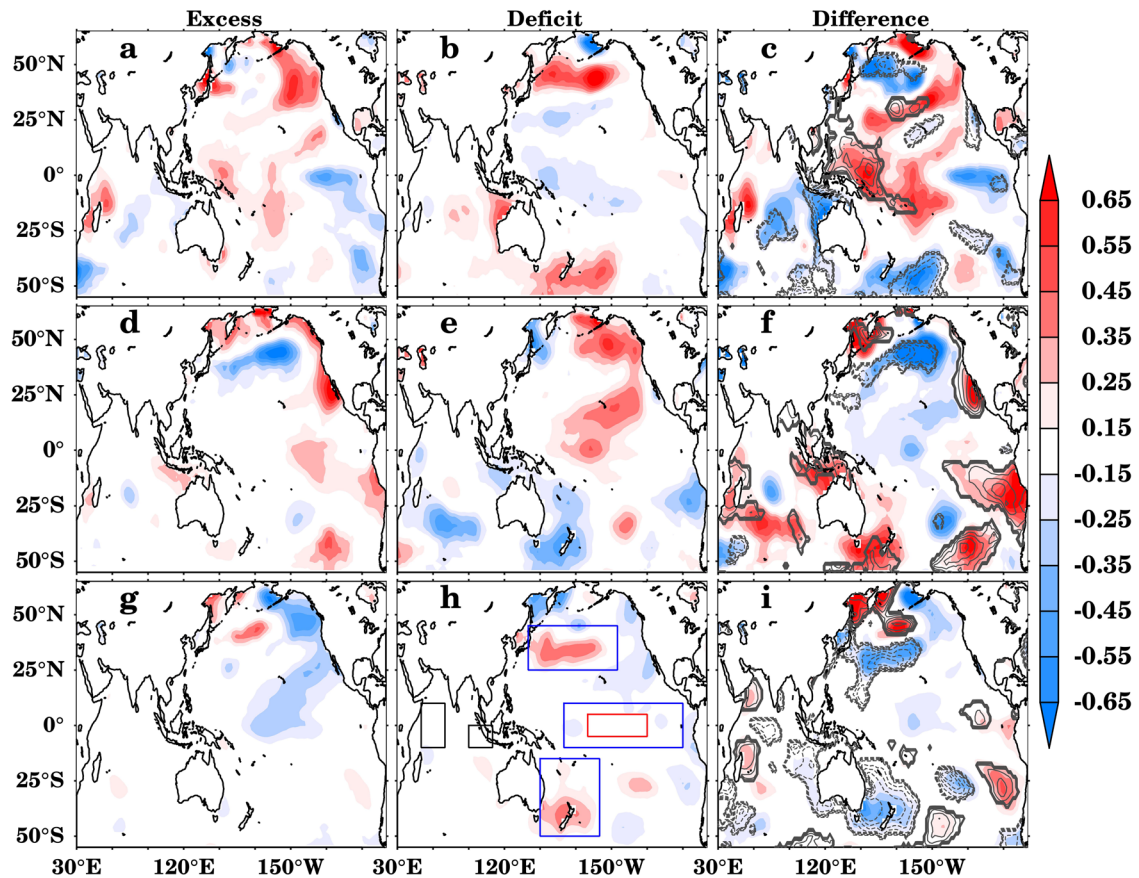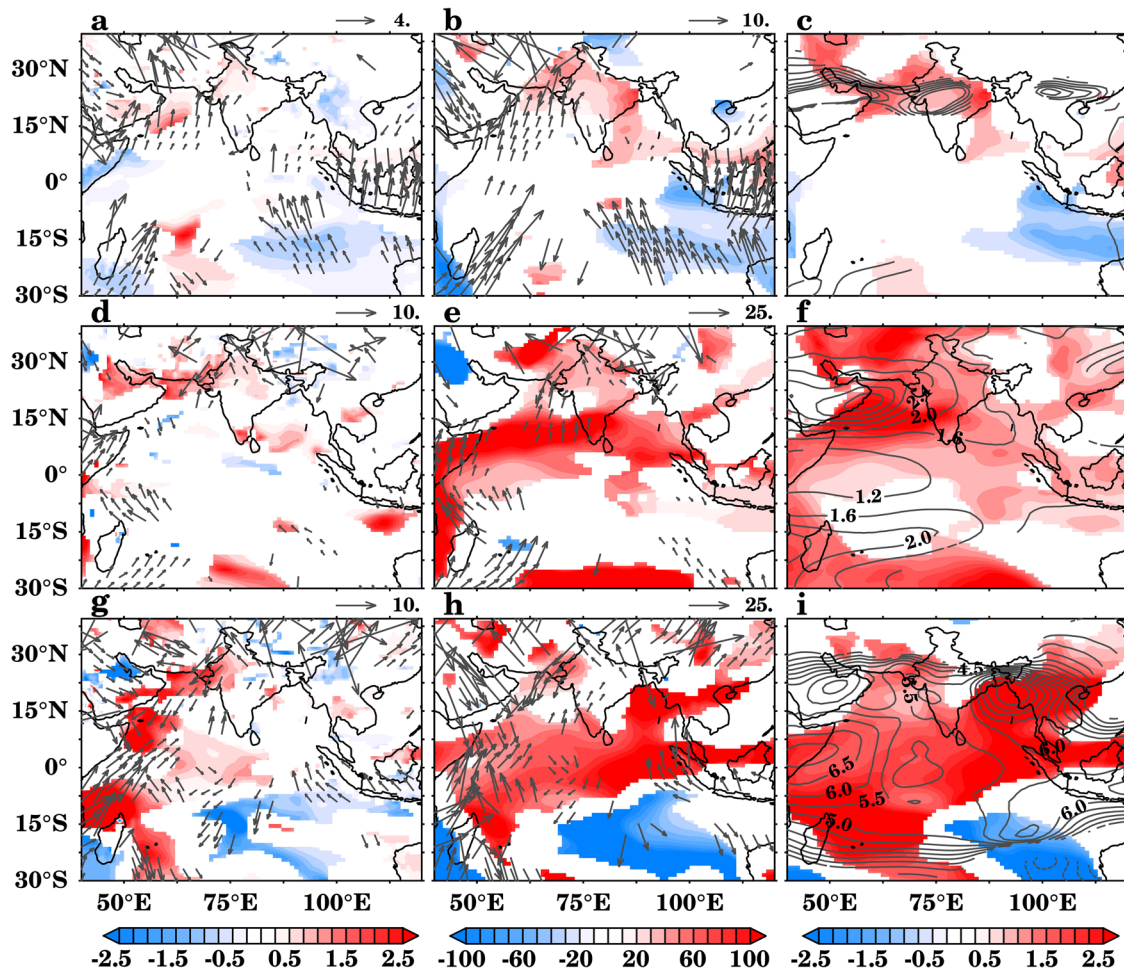
Fig. 4 Teleconnection of WG rainfall variability to Indo-Pacific SST. Composite of summer mean SSTA (°C) from ERSSTv5 for **a** excess, **b** deficit rainfall years and **c** difference (**a**, **b**) for period 1 (1901–1942). **d**, **e**, and **f** same as **a**, **b**, and **c** but for period 2 (1943–1977). **g**, **h**, and **i** same as **a**, **b**, and **c** but for period 3 (1978–2010). Contours in panels **c**, **f**, and **i** showing the correlation of filtered WGI with filtered SST at 90% confidence upon student *t*-test. Boxes in **h** are representing the area taken for calculating SST indices: Niño3.4 (red box), TPI (blue boxes), and DMI (black boxes).

deficit years, and difference. In excess (deficit) years, the MSE anomaly is positive (negative) throughout India and the surrounding region, which is also observed in the difference plot (Supplementary Fig. 7i). With all these fields, correlation analysis is also carried out with WGI for period 2 (Supplementary Fig. 5d–f), significant correlations are found with VIMT associated with monsoon and MSE; however, for winds, it shows a significant correlation over the Somali coast. Hence regression, correlation, and composite analysis are consistent with each other, indicating that compared to period 1, in period 2, apart from circulation, moisture content also displayed relative changes during the respective phases of WGI.

Figure 5g–i shows the regression of WGI with low-level wind anomaly, vertical velocity (Fig. 5g), with VIMT anomaly and VIM anomaly (Fig. 5h), with tropospheric temperature anomaly and MSE anomaly (Fig. 5i) for period 3. In the case of low-level wind opposite significant regression vectors indicate out of phase relation between WGI and low-level winds of the north of Somali in the AS, whereas VIM and MSE show significant positive regression over the north Indian Ocean and over the WG. Supplementary Fig. 8 shows composite analysis similar to Supplementary Fig. 6 but for period 3. The low-level wind (Supplementary Fig. 8a–c) is south south-easterly over WG associated with anti-cyclonic circulation over the Bay of Bengal (BoB), manifesting weaker monsoon low-level circulation for excess years (Supplementary Fig. 8a). In deficit years, the anti-cyclonic wind circulation is found over the AS and mostly northerly wind over WG (Supplementary Fig. 8b). In the difference, wind anomaly is southerly over WG, and anomalous cyclonic

circulation is reported off WG, which supports northward wind over WG (Supplementary Fig. 8c). The anomalous positive (negative) vertical wind is observed over WG region during excess (deficit) years. The VIMT anomaly shows the transport of moisture from east and south-east to WG during the positive phase, whereas during the negative phase, transport is from the north (Supplementary Fig. 8d, e). The corresponding VIM anomaly is positive for excess composite, indicating easterly and south-easterly bringing moisture-laden air for excess years, while northerly bringing dry air to the region and leads to negative VIM anomaly during deficit years. The VIM anomaly is positive over the entire domain except in the southern BoB in excess years and negative over WG, AS, and BoB in deficit years. The difference shows anomalous positive VIM throughout WG and adjacent areas. Their difference (Supplementary Fig. 8f) also displays twin cyclonic circulation around the equator near 60°E, and the northern one is relatively asymmetric with strong northward winds in the eastern flank which is on WG and east of it. This cyclonic circulation is favorable for enhancing convective activity supporting excess rainfall during the positive phase and vice versa for the negative phase. Supplementary Fig. 8g–i shows the composite of TT anomaly and mean MSE anomaly for excess, deficit years, and their difference respectively. During excess year composite (Supplementary Fig. 8g) mean MSE anomaly over the whole study region is positive, whereas, during deficit year composite (Supplementary Fig. 8h), an anomaly is negative over AS and the western part of India including WG region. The difference (Supplementary Fig. 8i) shows a high MSE anomaly in the AS and the western equatorial Indian Ocean. Correlation analysis is

Fig. 5 Association of WG rainfall variability to circulation and moist thermodynamical processes. Regression of WGI (mm/day) with anomaly of **a** wind vector (m/s) at 850 hPa and vertical wind at 500 hPa (shaded; mm/s). **b** Vertically integrated (1000–300 hPa) moisture transport (vector; kg/m.s) and vertically integrated moisture (shaded; kg/m²). **c** Tropospheric Temperature averaged over the 600–200 hPa (contour, °C) and moist static energy averaged over the 1000–200 hPa (shaded; kJ/kg) for period 1. **d, e, f** same as **a**, **b**, and **c** but for Period 2. **g**, **h**, **i** same as **a**, **b**, and **c** but for Period 3. Only values qualifies 90% confidence level are shown.

carried out with WGI filtered data for period 3 (Supplementary Fig. 5g–i), which shows a significant positive correlation with the VIMT and MSE associated with monsoon; however, for winds, it shows a significant correlation off the Somali coast. Hence correlation analysis is consistent with the composite analysis, which supports that MSE is in phase with the rainfall variability during period 3.

Figure 6 shows latitude-height section for the difference of excess and deficit year anomaly composite for zonal winds, MSE, and virtual temperature averaged over 70°E–73°E for respective periods, where contour display regression of particular filed with WGI. Figure 6a shows a positive zonal wind anomaly difference throughout the troposphere; indicates zonal wind anomaly is positive in the lower and middle troposphere and negative in the upper troposphere for excess composite, whereas for deficit composite (Supplementary Fig. 9a, b), opposite nature of zonal wind and wind speed anomaly is reported for period 1. Regression analysis with WGI for zonal wind reveals that coherent relation qualifies significant level with 90% confidence in the lower to midtroposphere. Corresponding MSE anomaly difference is also studied (Fig. 6b), weak positive anomaly north of 13°N (regression analysis also shows significant relation between WGI and MSE) is found for MSE while for the rest of the area it is negative. During deficit (excess) years, it is negative (positive) almost throughout the WG region (Supplementary Fig. 9c, d). Figure 6c shows the

difference in virtual temperature anomaly for excess and deficit rainfall years respectively. Weak negative (positive) anomalies are found between 800hPa to 600hPa for virtual temperature for excess (deficit) composites (Supplementary Fig. 9c, d), which are inconsistent with the rainfall anomaly. This analysis also supports that circulation features off WG display clear differences in excess and deficit year composite during the first period.

Figure 6d–f is for period 2, the zonal wind anomaly is positive with vertical extent up to 400 hPa for excess composite, whereas during the deficit composite, the zonal wind anomaly is negative and confined to the north of 15°N (Fig. 6d, Supplementary Fig. 10a, b). It is important to note that compared to period 1, wind anomalies for both the phases are less in period 2. Regression of zonal wind with WGI (Fig. 6d) shows a significant positive regression coefficient over the north of 17 °N only. MSE anomaly is positive for excess years composite and vice versa in deficit year composite (Fig. 6e, Supplementary Fig. 10c, d), and MSE displayed significant regression with WGI over almost the whole troposphere. Virtual temperature anomaly is positive in excess years and negative or almost zero during deficit years (Supplementary Fig. 10c, d), suggesting higher vapor pressure during excess years than deficit years and confirming that instability and convective activity is stronger in excess years than in deficit years. Regression analysis (Fig. 6f) shows significant relation between virtual temperature and WGI for mid to upper troposphere region.
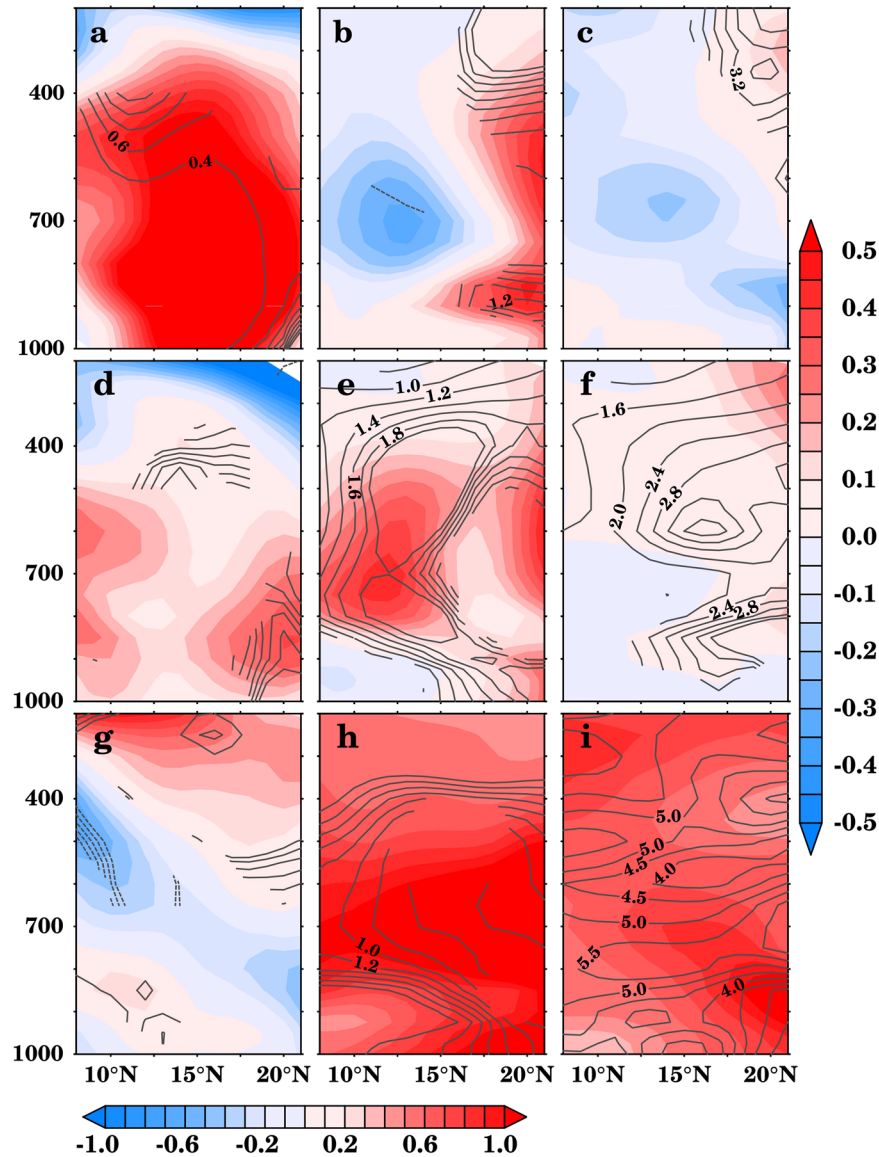
Fig. 6 Concurrent evolution of circulation and moist processes to WG rainfall variability in latitude-height section. Latitude-height section (averaged over 70°E–73°E) of **a** zonal wind (m/s), **b** MSE (kJ/kg), and **c** virtual temperature (°C) composite anomaly difference for excess to deficit years (shaded) and their regression with the WGI (contour, statistically signifcane at 90% confidence level) for period 1 and **d**–**f** and **g**–**i** are same but for period 2 and period 3, respectively.

Figure 6g–i, is for period 3, it is important to note that the zonal wind and wind speed for excess and deficit composite (Fig. 6g and Supplementary Fig. 11a, b) does not show major differences; they are negative in the lower to middle troposphere with small magnitude compared to period 1 and regression analysis does not show any strong significant relation with WGI. This indicates that the monsoon circulations of the WG and WG rainfall are relatively inconsistent during period 3. However, the MSE anomaly (Fig. 6h, Supplementary Fig. 11c, d) is positive and strongest for excess composite among all three periods and vice versa for deficit composite and regression with WGI is positive throughout the troposphere and significant with a confidence level of 90%. The positive anomalies of virtual temperature in excess years and negative anomalies in the deficit years leads to positive difference by more than 1 °C (Fig. 6i, Supplementary Fig. 11c, d), which endorse the presence of the higher amount of vapor in the atmosphere and convective instability during the positive phase and vice versa in the negative phase, which is resembled in the

regression analysis between WGI and virtual temperature. Hence analysis further supports that during period 3, monsoon circulation is not in line with WGI; however, monsoon moist thermodynamics is favorable with the observed rainfall variability. Thus during the recent period, moist thermodynamics processes are playing a dominant role in the WG rainfall decadal variability, while in period 1, the monsoon circulation/dynamics played a dominant role in the rainfall variability.

DISCUSSION

WG region receives more than 14 mm/day rainfall during the summer monsoon season; whereas, all-India averaged summer monsoon rainfall is about 7 mm/day[10]. The decadal and multidecadal-scale rainfall variability over the WG region remains unexplored. Recent release of century-long rainfall data by the GPCC, UDEL, and IMD, more than one and half-century-long SST analysis data from ERSSTv5, and century reanalysis data by
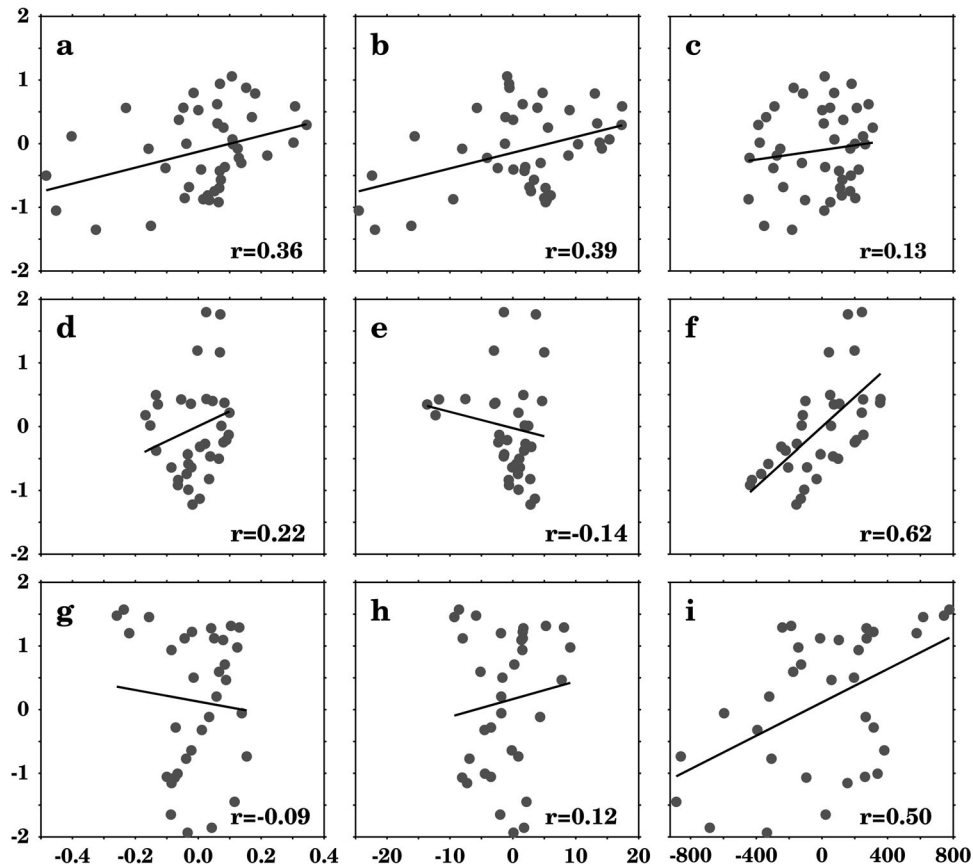
Fig. 7 Scatter analysis of WG rainfall variability against circulation and MSE. Scatter diagram of filtered anomalies of WG area-averaged (selected area shown in the Fig. 1) summer mean rainfall with summer mean **a** zonal wind (m/s) at 1000 hPa, **b** Relative Vorticity (*10^{-7} S^{-1}) at 1000 hPa, and **c** MSE (kJ/kg) averaged over the 1000–200 hPa for period 1; **d**, **e**, **f** for period 2 and **g**, **h**, **i** for period 3, respectively. The linear best fit line is overlaid in each panel.

National Oceanic and Atmospheric Administration (NOAA) gives an opportunity to study the decadal variability of rainfall and the associated processes. Spectrum and Wavelet analysis confirm the existence of decadal variability of rainfall over the WG, with a confidence level of 90%. Filter analysis of WG rainfall shows decadal rainfall variability with a strength of 1.6 mm/day, post 1950 period displayed enhancement of decadal variability amplitude by 1.5–2 fold compared to the previous half-century. The decadal-scale rainfall SST correlation shows variation with time, during 1901–1942, DMI indices show significant correlation with WG rainfall, while in 1943–1977, mostly PDO displayed a significant correlation with the WGI, whereas during the recent period (i.e., 1978–2010), PDO, IPO, and DMI showed significant in-phase relation. In contrast, TIO basin mode and AMO show out of phase relation.

The above analysis indicates that the decadal variability in WG rainfall undergoes changes in temporal correlation with dominant SST modes. This has motivated us to study the WG rainfall variability during three different periods, which are as follows: period 1 (1901–1942), period 2 (1943–1977), and period 3 (1978–2010). The spatial pattern of rainfall reveals that during period 1, decadal variability of rainfall was confined to southern WG (south of 16 °N), whereas, during periods 2 and 3, the whole WG region shows decadal variability of rainfall with amplitude 3 to 6 mm/day. Corresponding regression, correlation, and composite analysis of monsoon circulation and moisture fields with WG ranfall decadal variability are studied for each period respectively. During period 1, monsoon circulation is in phase with the WG rainfall decadal variability; however, moisture fields are relatively weak and inconsistent. In the case of periods 2 and 3, circulation fields are weaker/inconsistent with the rainfall decadal variability, but moisture fields are consistent with the rainfall decadal variability of WG regions.

Figure 7 shows a scatter diagram of 1000 hPa zonal wind anomaly (Fig. 7a, d, g), 1000 hPa vorticity anomaly (Fig. 7b, e, h), and mean MSE anomaly (Fig. 7c, f, i) with rainfall anomaly for different periods separately. The rainfall during period 1 displays a positive correlation with 1000 hPa zonal wind (Fig. 7a, r = 0.36) and relative vorticity (Fig. 7b, r = 0.39), but the mean MSE shows poor correlation (Fig. 7c). During period 2, the correlation of 1000 hPa zonal wind has reduced (Fig. 7d, r = 0.22), also a similar relation is observed for the 1000 hPa relative vorticity (Fig. 7e). The mean MSE (Fig. 7f) contributed to rainfall with the correlation of 0.62, supporting that the rainfall variability is consistent with the moisture variability. Similarly, in period 3 also, the rainfall has a correlation of 0.50 with mean MSE (Fig. 7i), and the correlation with 1000 hPa zonal wind (Fig. 7g) and vorticity (Fig. 7h) is less. This further confirms that rainfall variability during periods 2 and 3 is coherent with moist thermodynamic processes, whereas rainfall variability in period 1 is dynamically driven. The present study concludes that decadal variability of rainfall over WG region is robust, and its relation with dominant SST decadal modes has temporal variations. Identification of decadal rainfall variability over WG and associated processes may add value to decadal prediction. In addition, it may help to understand the evolution of WG ecosystem and runoff variability of the southeastern Indian rivers.

METHODS

We used ERSSTv5 monthly SST analysis data[48–50] from the NOAA with a resolution of $2° \times 2°$ for the period 1900–2018. The updates incorporated in ERSSTv5 have improved the representation of spatial variability over the global oceans, the magnitude of El Niño and La Niña events, and the decadal nature of SST changes over the 1930s–40s when observation instruments changed rapidly[50]. To know the mechanism behind WG rainfall variability, TIO index, Niño 3.4 index, and DMI for IOD are calculated from the ERSSTv5 dataset. IPO, PDO, AMO index are taken from NOAA Physical Sciences Laboratory. The area considered to estimate DMI, TPI, and Niño3.4 indices is provided in Fig. S1.

Precipitation dataset from the UDEL (version 4.01, $0.5° \times 0.5°$ resolutions) for the period 1900–2014 has been used. The UDEL Precipitation dataset version 4.01 uses the Global Historical Climatology Network and annual and monthly mean station observations of total precipitation[51]. In addition, GPCC full data reanalysis[52,53] version 2018, $0.5° \times 0.5°$, monthly data available from 1891 through 2016 is used. IMD has brought out a high-resolution ($0.25° \times 0.25°$) daily gridded rainfall dataset[54–56] for the period 1900– present using stations' observations. Many monsoon-related studies[3,31,57–59] used this dataset. Since the present analysis uses a fixed rainfall network, it examines long-term rainfall climate variability like decadal variability. This daily data are averaged for the summer monsoon (June to September) to get seasonal mean data for the study. Vertical profiles of temperature, zonal wind, meridional wind, wind speed, specific humidity, and geopotential have been used from Twentieth Century Reanalysis version 3 which is produced and supported by the NOAA, the Cooperative Institute for Research in Environmental Sciences, and the U.S. Department of Energy (NOAA20CRv3). NOAA20CRv3 uses upgraded data assimilation methods, including an adaptive inflation algorithm; higher-resolution forecast model; and assimilates a larger set of pressure observations which improved the ensemble-based estimates of confidence, removed spin-up effects in the precipitation fields, and diminished sea-level pressure bias; improved more minor errors, reduced large-scale model bias[60]. For all of the datasets used in this study, an anomaly is computed by subtracting the long-term mean, and the linear trend removed by detrending the data to remove the signal due to climate change. Power spectrum analysis is done to know the dominant frequency of variability in WG precipitation Index. The wavelet analysis is also carried out to get accurate localized time depending on frequency information. The wavelet analysis used the Morlet function, which detects both the phase and the time-dependent amplitude[61]. 9–30 years bandpass filter is applied on detrended anomaly to extract the decadal to the multidecadal signal of variability. We defined the WGI as the area average summer mean detrended precipitation anomaly over the WG region enclosed by the following coordinates {(72.5°E, 21.5°N), (72.5°E, 18.0°N), (74.5°E, 13.0°N), (76.5°E, 8.5°N), (77.5°E, 9.0°N), (76.5°E, 13.0°N), (74.5°E, 18.0°N), (74.5°E, 21.5°N), (72.5°E, 21.5°N)}. The selected area is denoted with the dashed line in Fig. 1f. WGI from different datasets shows the correlation between them is greater than 0.9 (Fig. 2a, d), confirming the robustness of the WGI in all the precipitation datasets used in this study. It is important to note that all the regression, correlation, and composite analyses carried out for diagnosis, used a bandpass filtered (9–30 years) dataset for each variable. To know the relation between WGI and SST indices, 31 years of moving correlation analysis is carried out. From WGI filtered time-series (Fig. 2d), excess and deficit years are identified for composite analysis. WGI regression/correlation with SSTA, low-level winds anomaly, vertical wind anomaly at 500hPa, moisture fields anomaly, and troposphere temperature fields anomaly is also studied. For process studies, MSE[62] VIM, VIMT[31,63], and virtual temperature[64] are calculated. TT is computed using air temperature data[44].

DATA AVAILABILITY

The ERSSTv5 analysis, IMD rainfall, and NOAA 20th Century reanalysis gridded datasets are downloaded, respectively, from https://www.ncei.noaa.gov/pub/data/cmb/ersst/v5/netcdf/, https://www.imdpune.gov.in/Clim_Pred_LRF_New/Grided_Data_Download.html, and https://psl.noaa.gov/data/gridded/data.20thC_ReanV3.html. GPCC Precipitation data are provided by the NOAA/OAR/ESRL PSL, Boulder, Colorado, USA, from their Web site https://www.psl.noaa.gov/data/gridded/data.gpcc.html.

REFERENCES

1. Naidu, P. D. et al. Coherent response of the Indian Monsoon Rainfall to Atlantic Multi-decadal Variability over the last 2000 years. *Sci. Rep.* **10**, 1302, https://doi.org/10.1038/s41598-020-58265-3 (2000).
2. Dwivedi, S. et al. New spatial and temporal indices of Indian summer monsoon rainfall. *Theor. Appl. Climatol.* **135**, 979–990 (2019).
3. Vibhute, A. et al. Decadal variability of tropical Indian Ocean sea surface temperature and its impact on the Indian summer monsoon. *Theor. Appl. Climatol.* **141**, 551–566 (2020).
4. Walker, G. T. Correlation in seasonal variation of weather. VIII: A preliminary study of world weather. *Mem. Indian Meteorol. Dep.* **24**, 75–131 (1923).
5. Walker, G. T. Correlations in seasonal variations of weather. IX. A further study of world weather. *Mem. Indian Meteorol. Dep.* **24**, 275–332 (1924).
6. Sikka, D. R. Some aspects of the large scale fluctuations of summer monsoon rainfall over India in relation to fluctuations in the planetary and regional scale circulation parameters. *Proc. Indian Acad. Sci. Earth Planet. Sci.* **89**, 179–195 (1980).
7. Rasmusson, E. M. & Carpenter, T. H. The relationship between eastern equatorial Pacific sea surface temperatures and rainfall over India and Sri Lanka. *Mon. Weather Rev.* **111**, 517–528 (1983).
8. Mooley, D. A. & Parthasarathy, B. Fluctuations in All-India summer monsoon rainfall during 1871–1978. *Clim. Change* **6**, 287–301 (1984).
9. Rajeevan, M. & McPhaden, M. J. Tropical Pacific upper ocean heat content variations and Indian summer monsoon rainfall. *Geophys. Res. Lett.* **31**, 1–4, https://doi.org/10.1029/2004GL020631 (2004).
10. Kulkarni, A. et al. Precipitation changes in India. *Assess. Clim. Change Indian Reg. Rep. Minist. Earth Sci. MoES Gov. India* https://doi.org/10.1007/978-981-15-4327-2_3 (2020).
11. Sehgal, K. L. Coldwater fish and fisheries in the Western Ghats, India. *Fish. Fish. High. Alt. Asia* **385**, 103–103 (1999).
12. Jain, S. K., Agarwal, P. K. & Singh, V. P. In *Hydrology and water resources of India*. vol. 57 (Springer Science & Business Media, 2007).
13. "Western Ghats", World Heritage Convention. *United Nations Educational, Scientific and Cultural Organization (UNESCO)*. https://whc.unesco.org/en/list/1342/ (2012).
14. Grossman, R. L. & Durran, D. R. Interaction of low-level flow with the Western Ghat mountains and offshore convection in the summer monsoon. *Mon. Weather Rev.* **112**, 652–672 (1984).
15. Xie, S. P., Xu, H., Saji, N. H., Wang, Y. & Liu, W. T. Role of narrow mountains in large-scale organization of Asian Monsoon convection. *J. Clim.* **19**, 3420–3429 (2006).
16. Tripti, M. et al. Water circulation and governing factors in humid tropical river basins in the central Western Ghats, Karnataka, India. *Rapid Commun. Mass Spectrom.* **30**, 175–190 (2016).
17. Varikoden, H., Revadekar, J. V., Kuttippurath, J. & Babu, C. A. Contrasting trends in southwest monsoon rainfall over the Western Ghats region of India. *Clim. Dyn.* **52**, 4557–4566 (2019).
18. Prakash, S., Sathiyamoorthy, V., Mahesh, C. & Gairola, R. M. Is summer monsoon rainfall over the west coast of India decreasing? *Atmos. Sci. Lett.* **14**, 160–163 (2013).
19. Rao, Y. P. *Meteorological monograph, Synoptic-Meteorology No. 1/1976. Southwest Monsoon*. https://www.imdpune.gov.in/Weather/Reports/swmonsoonwholebook.pdf. (1976).
20. Sarker, R. P. Some modifications in a dynamical model of orographic rainfall. *Mon. Weather Rev.* **95**, 673–684 (1967).
21. Venkatesh, B. & Jose, M. K. Identification of homogeneous rainfall regimes in parts of Western Ghats region of Karnataka. *J. Earth Syst. Sci.* **116**, 321–329 (2007).
22. Revadekar, J. V., Varikoden, H., Murumkar, P. K. & Ahmed, S. A. Latitudinal variation in summer monsoon rainfall over Western Ghat of India and its association with global sea surface temperatures. *Sci. Total Environ.* **613–614**, 88–97 (2018).
23. Soman, M. K. & Kumar, K. K. Some aspects of daily rainfall distribution over India during the south-west monsoon season. *Int. J. Climatol.* **10**, 299–311 (1990).
24. Mooley, D. A. Major climatological discontinuities in the monthly monsoon activity in the neightbourhood of theWestern Ghats. *MAUSAM* **29**, 508–514 (1978).
25. Sarker, R. P. A dynamical model of orographic rainfall. *Mon. Weather Rev.* **94**, 555–572 (1966).
26. Ogura, Y. & Yoshizaki, M. Numerical study of orographic-convective precipitation over the eastern Arabian Sea and the Ghat Mountains during the summer monsoon. *J Atmos Sci.* **45**, 2097–2122 (1988).
27. Patwardhan, S. K. & Asnani, G. C. Meso-scale distribution of summer monsoon rainfall near the Western Ghats (India). *Int. J. Climatol.* **20**, 575–581 (2000).
28. Kumar, U. M., Swain, D., Sasamal, S. K., Reddy, N. N. & Ramanjappa, T. Validation of SARAL/AltiKa significant wave height and wind speed observations over the North Indian Ocean. *J. Atmos. Sol. Terr. Phys.* **135**, 174–180 (2015).

29. Naidu, C. V. et al. Is summer monsoon rainfall decreasing over India in the global warming era? *J. Geophys. Res. Atmos.* **114**, 1–16, https://doi.org/10.1029/2008JD011288 (2009).

30. Krishnakumar, K. N., Prasada Rao, G. S. L. H. V. & Gopakumar, C. S. Rainfall trends in twentieth century over Kerala, India. *Atmos. Environ.* **43**, 1940–1944 (2009).

31. Konwar, M., Parekh, A. & Goswami, B. N. Dynamics of east-west asymmetry of Indian summer monsoon rainfall trends in recent decades. *Geophys. Res. Lett.* **39**, 1–6, https://doi.org/10.1029/2012GL052018 (2012).

32. Varikoden, H., Kumar, K. K. & Babu, C. A. Long term trends of seasonal and monthly rainfall in different intensity ranges over Indian subcontinent. *MAUSAM* **64**, 481–488 (2013).

33. Preethi, B., Mujumdar, M., Kripalani, R. H., Prabhu, A. & Krishnan, R. Recent trends and tele-connections among South and East Asian summer monsoons in a warming environment. *Clim. Dyn.* **48**, 2489–2505 (2017).

34. Joshi, M. K. & Pandey, A. C. Trend and spectral analysis of rainfall over India during 1901-2000. *J. Geophys. Res. Atmos.* **116**, 1–13, https://doi.org/10.1029/2010JD014966 (2011).

35. Deepa, J. S. & Gnanaseelan, C. The decadal sea level variability observed in the Indian Ocean tide gauge records and its association with global climate modes. *Glob. Planet. Change* **198**, 103427–103427 (2021).

36. Henley, B. J. et al. A tripole index for the interdecadal Pacific oscillation. *Clim. Dyn.* **45**, 3077–3090 (2015).

37. Mantua, N. J., Hare, S. R., Zhang, Y., Wallace, J. M. & Francis, R. C. A Pacific interdecadal climate oscillation with impacts on Salmon production*. *Bull. Am. Meteorol. Soc.* **78**, 1069–1080 (1997).

38. Schlesinger, M. E. & Ramankutty, N. An oscillation in the global climate system of period 65–70 years. *Nature* **367**, 723–726 (1994).

39. Halder, S., Parekh, A., Chowdary, J. S., Gnanaseelan, C. & Kulkarni, A. Assessment of CMIP6 models' skill for tropical Indian Ocean sea surface temperature variability. *Int. J. Climatol.* **41**, 2568–2588 (2021).

40. Hua, W., Dai, A. & Qin, M. Contributions of internal variability and external forcing to the recent Pacific decadal variations. *Geophys. Res. Lett.* **45**, 7084–7092 (2018).

41. Ashok, K., Guan, Z. & Yamagata, T. Impact of the Indian Ocean dipole on the relationship between the Indian monsoon rainfall and ENSO. *Geophys. Res. Lett.* **28**, 4499–4502 (2001).

42. Matsuno, T. Quasi-Geostrophic motions in the equatorial area. *J. Meteorol. Soc. Jpn. Ser. II* **44**, 25–43 (1966).

43. Gill, A. E. Some simple solutions for heat-induced tropical circulation. *Q. J. R. Meteorol. Soc.* **106**, 447–462 (1980).

44. Xavier, P. K., Marzin, C. & Goswami, B. N. An objective definition of the Indian summer monsoon season and a new perspective on the ENSO-monsoon relationship. *Q. J. R. Meteorol. Soc.* **133**, 749–764 (2007).

45. Flohn, H. Large-scale aspects of the "Summer Monsoon" in South and East Asia. *J. Meteorol. Soc. Jpn. Ser. II* **35A**, 180–186 (1957).

46. Liu, X. & Yanai, M. Relationship between the Indian monsoon rainfall and the tropospheric temperature over the Eurasian continent. *Q. J. R. Meteorol. Soc.* **127**, 909–937 (2001).

47. Flohn, H. Recent investigations on the mechanism of the "'summer monsoon'" of southern and eastern Asia. In: Basu S, Ramanathan KR, Pisharoty PR, Bose UK (eds) Monsoons of the World. India Meteorological Department, Delhi, pp 75–88 (1960).

48. Smith, T. M., Reynolds, R. W., Livezey, R. E. & Stokes, D. C. Reconstruction of historical sea surface temperatures using empirical orthogonal functions. *J. Clim.* **9**, 1403–1420 (1996).

49. Smith, T. M. & Reynolds, R. W. Extended reconstruction of global sea surface temperatures based on COADS data (1854–1997). *J. Clim.* **16**, 1495–1510 (2003).

50. Huang, B. et al. Extended reconstructed Sea surface temperature, Version 5 (ERSSTv5): Upgrades, validations, and intercomparisons. *J. Clim.* **30**, 8179–8205 (2017).

51. Matsuura, K. & Willmott, C. J. Terrestrial air temperature: 1900–2008 gridded monthly time series. *Cent. Clim. Res. Dep Geogr. Univ. Del. Newark Httpclimate Geog Udel Edu Clim.* http://climate.geog.udel.edu/~climate/html_pages/Global2_Ts_2009/README.global_p_ts_2009.html (2009).

52. Schneider, U. et al. *GPCC full data reanalysis version 6.0 at 0.5: monthly land-surface precipitation from rain-gauges built on GTS-based and historic data.* https://doi.org/10.5676/DWD_GPCC (2011).

53. Schneider, U. et al. Evaluating the hydrological cycle over land using the newly-corrected precipitation climatology from the Global Precipitation Climatology Centre (GPCC). *Atmosphere* **8**, 1–17, https://doi.org/10.3390/atmos8030052 (2017).

54. Rajeevan, M., Bhate, J., Kale, J. D. & Lal, B. High resolution daily gridded rainfall data for the Indian region: Analysis of break and active monsoon spells. *Curr. Sci.* **91**, 296–306 (2006).

55. Rajeevan, M. & Bhate, J. A high resolution daily gridded rainfall dataset (1971-2005) for mesoscale meteorological studies. *Curr. Sci.* **96**, 558–562 (2009).

56. Pai, D. S. et al. Development of a new high spatial resolution (0.25° × 0.25°) long period (1901–2010) daily gridded rainfall data set over India and its comparison with existing data sets over the region. *MAUSAM* **65**, 1–18 (2014).

57. Goswami, B. N., Madhusoodanan, M. S., Neema, C. P. & Sengupta, D. A physical mechanism for North Atlantic SST influence on the Indian summer monsoon. *Geophys. Res. Lett.* **33**, 2706–2706 (2006).

58. Krishnamurthy, V. & Shukla, J. Seasonal persistence and propagation of intra-seasonal patterns over the Indian monsoon region. *Clim. Dyn.* **30**, 353–369 (2008).

59. Ajayamohan, R. S. & Rao, S. A. Indian ocean dipole modulates the number of extreme rainfall events over India in a warming environment. *J. Meteorol. Soc. Jpn.* **86**, 245–252 (2008).

60. Slivinski, L. C. et al. Towards a more reliable historical reanalysis: Improvements for version 3 of the Twentieth Century Reanalysis system. *Q. J. R. Meteorol. Soc.* **145**, 2876–2908 (2019).

61. Torrence, C. & Compo, G. P. A practical guide to wavelet analysis. *Bull. Am. Meteorol. Soc.* **79**, 61–78 (1998).

62. Attada, R., Parekh, A., Chowdary, J. S. & Gnanaseelan, C. Reanalysis of the Indian summer monsoon: four dimensional data assimilation of AIRS retrievals in a regional data assimilation and modeling framework. *Clim. Dyn.* **50**, 2905–2923 (2018).

63. Fasullo, J. & Webster, P. J. A hydrological definition of Indian monsoon onset and withdrawal. *J. Clim.* **16**, 3200–3211 (2003).

64. Danard, M. A note on the effects of virtual temperature: research note. *Atmos. Ocean* **32**, 485–493 (1994).

ACKNOWLEDGEMENTS

AUTHOR CONTRIBUTIONS

A.P. and S.H. designed and conceived the study, S.H. and A.P. conducted the analysis and interpreted the results. S.H., A.P., J.S.C., and C.G. have contributed to the discussions as well as in manuscript writing.

COMPETING INTERESTS

The authors declare no competing interests.

ADDITIONAL INFORMATION

Supplementary information The online version contains supplementary material available at https://doi.org/10.1038/s41612-022-00232-y.

Correspondence and requests for materials should be addressed to Subrota Halder.

Reprints and permission information is available at http://www.nature.com/reprints

Publisher's note Springer Nature remains neutral with regard to jurisdictional claims in published maps and institutional affiliations.